remote sensing

MDPI

Article

Frequency-Wavenumber Domain Elastic Full Waveform Inversion with a Multistage Phase Correction

Yong Hu [1,2], Li-Yun Fu [2,*], Qingqing Li [2], Wubing Deng [2] and Liguo Han [3]

[1] School of Resources and Geosciences, China University of Mining and Technology, Xuzhou 221008, China
[2] Shandong Provincial Key Laboratory of Deep Oil and Gas, China University of Petroleum (East China), Qingdao 266580, China
[3] College of Geo-Exploration Science and Technology, Jilin University, Changchun 130026, China
* Correspondence: lfu@upc.edu.cn

Abstract: Elastic full waveform inversion (EFWI) is essential for obtaining high-resolution multi-parameter models. However, the conventional EFWI may suffer from severe cycle skipping without the low-frequency components in elastic seismic data. To solve this problem, we propose a multistage phase correction-based elastic full waveform inversion method in the frequency-wavenumber domain, which we call PC-EFWI for short. Specifically, the seismic data are first split using 2-D sliding windows; for each window, the seismic data are then transformed into the frequency-wavenumber domain for PC-EFWI misfit. In addition, we introduced a phase correction factor in the PC-EFWI misfit. In this way, it is possible to reduce phase differences between measured and synthetic data to mitigate cycle skipping by adjusting the phase correction factor in different scales. Numerical examples with the 2-D Marmousi model demonstrate that the frequency-wavenumber domain PC-EFWI with multistage strategy is an excellent way to reduce the risk of EFWI cycle skipping and build satisfactory start models for the conventional EFWI.

Keywords: elastic full waveform inversion; frequency-wavenumber domain; multistage phase correction; cycle skipping; multi-parameter

Citation: Hu, Y.; Fu, L.-Y.; Li, Q.; Deng, W.; Han, L. Frequency-Wavenumber Domain Elastic Full Waveform Inversion with a Multistage Phase Correction. *Remote Sens.* **2022**, *14*, 5916. https://doi.org/10.3390/rs14235916

Academic Editors: Jingrui Luo and Benfeng Wang

Received: 28 October 2022
Accepted: 18 November 2022
Published: 22 November 2022

1. Introduction

The characterization of the velocity models is significant for improving seismic migration and geology interpretation [1–5]. Full waveform inversion (FWI) uses the kinematic and dynamic information of seismic waves and is considered an effective means for velocity model building [6–10]. However, the characteristics of the FWI misfit show strong nonlinearity [11–17]. Suppose the seismic data lack low-frequency components and the background velocity is very different from the accurate model. In that case, the FWI misfit may be trapped in local minima, leading to severe cycle skipping [18–23]. In addition, the physical properties of the subsurface are very complex, and the acoustic wave equation-based FWI cannot correctly obtain the multi-parameter models [11,24–28]. Therefore, given the quality of existing seismic data, the proposed new strategy and method comprise an important way to solve cycle skipping for FWI.

The cycle skipping destroys the advantage of high-resolution acoustic FWI and elastic FWI, which has attracted wide attention [29–33]. In recent years, many new methods and strategies have been proposed to mitigate cycle skipping of FWI by building a better initial model. The multiscale strategy is commonly used for FWI to obtain high-resolution velocity models [8,34–37]. However, the low-frequency seismic data are usually costly and contaminated by noise, leading to a multiscale strategy that usually does not work.

The envelope contains abundant low-frequency components, which is suitable for building the low-wavenumber velocity models [38–44]. Furthermore, a phase-tracking method can recover the missing low-frequency signals [45]. In addition, the Beat tone strategy [29], deconvolution method [46–49], and deep learning [50–53] also can be used to

recover the low-frequency components and for FWI to invert the macro structures of the subsurface. Similarly, reducing waveform mismatch can better alleviate the cycle skipping problem and make it easier for misfit to converge to the global minimum. Adaptive waveform inversion computes the matching filter instead of waveform differences [54]. An adaptive matching filter-based misfit can obtain the velocity model macro structures for the conventional FWI [55–57]. Ensemble Kalman filter also can be used to enlarge the convergence domain of the FWI misfit and alleviate the model dependence of the FWI method [24,58]. Therefore, whether low-frequency reconstruction or by modifying the phase or amplitude information of seismic data, the nonlinearity of FWI misfit can be effectively reduced. Then, the cycle skipping of FWI can be mitigated [59–62].

This article proposes a multistage phase correction-based elastic full waveform inversion (PC-EFWI) in the frequency-wavenumber domain. The PC-EFWI can effectively mitigate the cycle skipping by reducing phase differences between the measured and synthetic data. In the EFWI misfit, a phase correction factor is adopted to adjust phase differences. Suppose we eliminate the phase differences between the measured and synthetic data. In that case, the PC-EFWI misfit only contains the amplitude information, which is similar to the envelope inversion. However, If the phase correction factor is zero, the PC-EFWI misfit will degenerate into the conventional EFWI misfit. Therefore, we need to adjust the phase correction factor to bridge the inversion gap between the envelope inversion and waveform inversion results. Specifically, the article is organized as follows. We first extend the utilization of 2-D sliding windows to obtain windowed seismic data and give some theoretical formulas for a window-based 2-D Fourier transform. Then, we present the theory of the conventional elastic FWI. After that, the frequency-wavenumber domain PC-EFWI misfit and its gradient operators are established. Finally, in the numerical tests, the PC-EFWI results are regarded as the initial models for the conventional EFWI to invert the detailed structures.

2. Window-Based Frequency-Wavenumber Domain Phase Correction

In this section, we try to utilize a window-based 2-D Fourier transform to develop a frequency-wavenumber domain phase correction-based elastic full waveform inversion (PC-EFWI). In this case, we first need to define a window-based 2-D Fourier transform,

$$\begin{cases} \tilde{\mathbf{u}}(\tau,\ h,\ \omega,\ k_x) = F_{2D}[\mathbf{u}(t,x)] = \iint \mathbf{u}(t,x)\ \mathbf{g}(t-\tau, x-h)\ e^{-i(\omega t - k_x x)} dt\ dx \\ \mathbf{u}(t,x) = F_{2D}^{*}[\tilde{\mathbf{u}}(\tau,\ h,\ \omega,\ k_x)] = \iint \iint \tilde{\mathbf{u}}(\tau,\ h,\ \omega,\ k_x)\ \mathbf{g}(t-\tau, x-h) e^{i(\omega t - k_x x)}\ d\omega\ dk_x\ d\tau\ dh \end{cases} \tag{1}$$

where $F_{2D}[\,\cdot\,]$ and $F_{2D}^{*}[\,\cdot\,]$ mean the window-based 2-D Fourier forward and inverse transform, $\omega = 2\pi f$, f means the frequency, k_x is the wavenumber in x direction; $\mathbf{u}(t,x)$ are the seismic data, $\mathbf{g}(t,x)$ is a 2-D sliding window, $\tilde{\mathbf{u}}(\tau,\ h,\ \omega,\ k_x)$ are the window-based frequency-wavenumber domain seismic data; and τ and h are the displacements of t and x, respectively.

The seismic data can easily be separated into phase and amplitude components in the frequency-wavenumber domain as follows,

$$\begin{cases} \tilde{\mathbf{u}}(\tau,\ h,\ \omega,\ k_x) = \left|\tilde{\mathbf{u}}(\tau,\ h,\ \omega,\ k_x)\right| e^{i\psi_u} \\ \tilde{\mathbf{d}}(\tau,\ h,\ \omega,\ k_x) = \left|\tilde{\mathbf{d}}(\tau,\ h,\ \omega,\ k_x)\right| e^{i\psi_d} \end{cases}, \tag{2}$$

where $\tilde{\mathbf{u}}$, $\tilde{\mathbf{d}}$ are the frequency-wavenumber domain synthetic and measured data, respectively. Therefore, the phase differences between $\tilde{\mathbf{u}}$ and $\tilde{\mathbf{d}}$ can be denoted as follows,

$$e^{i(\psi_d - \psi_u)} = e^{i\Delta\psi} = \frac{\tilde{\mathbf{u}}^{*}\tilde{\mathbf{d}}}{\left|\tilde{\mathbf{u}}\right|\left|\tilde{\mathbf{d}}\right|}, \tag{3}$$

where ψ_u, ψ_d are the phase information in the frequency-wavenumber domain. In this way, the phase correction can denoted as,

$$\begin{cases} \tilde{\mathbf{u}}_c = \tilde{\mathbf{u}}\, e^{i\varepsilon(\psi_d - \psi_u)} \\ \tilde{\mathbf{d}}_c = \tilde{\mathbf{d}}\, e^{i\varepsilon(\psi_u - \psi_d)} \end{cases}, \tag{4}$$

where ε is a phase correction factor that controls the phase correction amount. If $\varepsilon = 0.5$, there are no phase differences between the corrected measured and synthetic data ($\mathrm{Im}\left[\ln\left(\tilde{\mathbf{u}}_c\right)\right] = \mathrm{Im}\left[\ln\left(\tilde{\mathbf{d}}_c\right)\right]$). If $\varepsilon = 0$, it has $\tilde{\mathbf{u}}_c = \tilde{\mathbf{u}}$, $\tilde{\mathbf{d}}_c = \tilde{\mathbf{d}}$. Therefore, it is possible to adjust the phase differences between the corrected measured and synthetic data using the phase correction factor.

The horizontal component of the measured elastic seismic data and the 2-D window are shown in Figure 1. In this case, we first use sliding windows to split seismic data and obtain Figure 2a,d. Equation (1) is then used to obtain the frequency-wavenumber domain seismic data. After that, we set $\varepsilon = 0.5$ with Equation (4), and we can obtain the phase-corrected seismic data. In addition, we also show the phase-corrected seismic waveforms in Figure 3. Comparing the original waveforms and phase-corrected waveforms demonstrates that the frequency-wavenumber domain phase correction strategy can effectively reduce the phase differences between the measured and synthetic data.

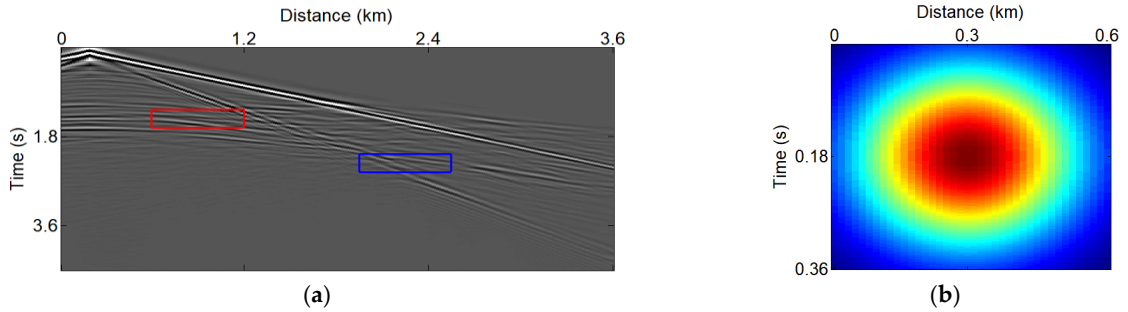

Figure 1. (**a**) Horizontal component of the measured elastic seismic data; (**b**) 2-D window.

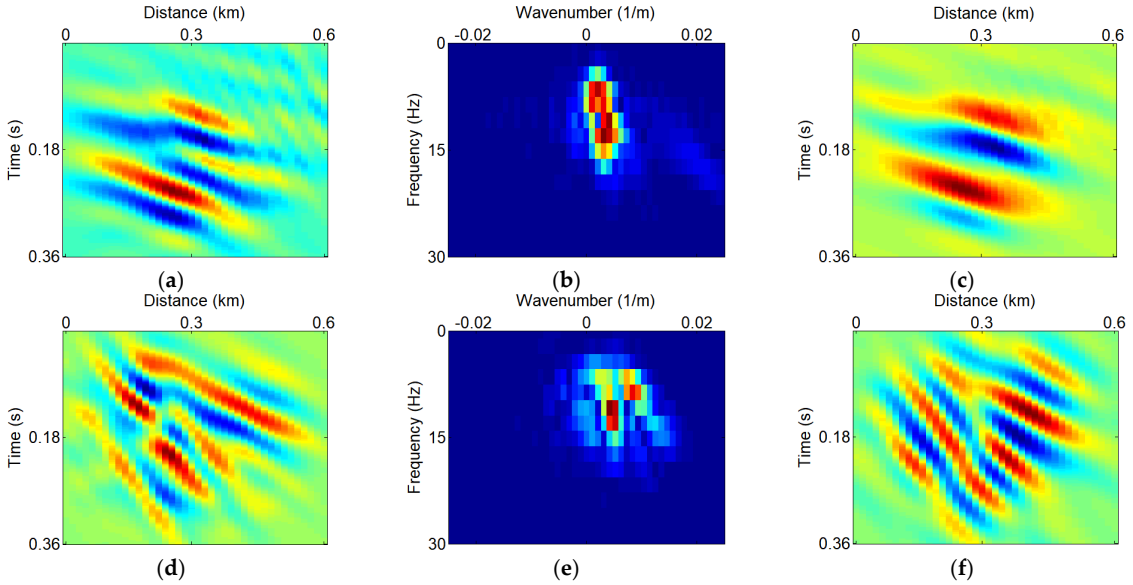

Figure 2. Windowed seismic data in the time-space domain and frequency-wavenumber domain; (**a**,**c**) are extracted from the red and blue rectangular boxes of Figure 1, respectively; (**b**,**e**) are the frequency-wavenumber domain amplitude information of (**a**,**d**), respectively; (**c**,**f**) are the phase-corrected seismic data of (**a**,**d**) with $\varepsilon = 0.5$, respectively.

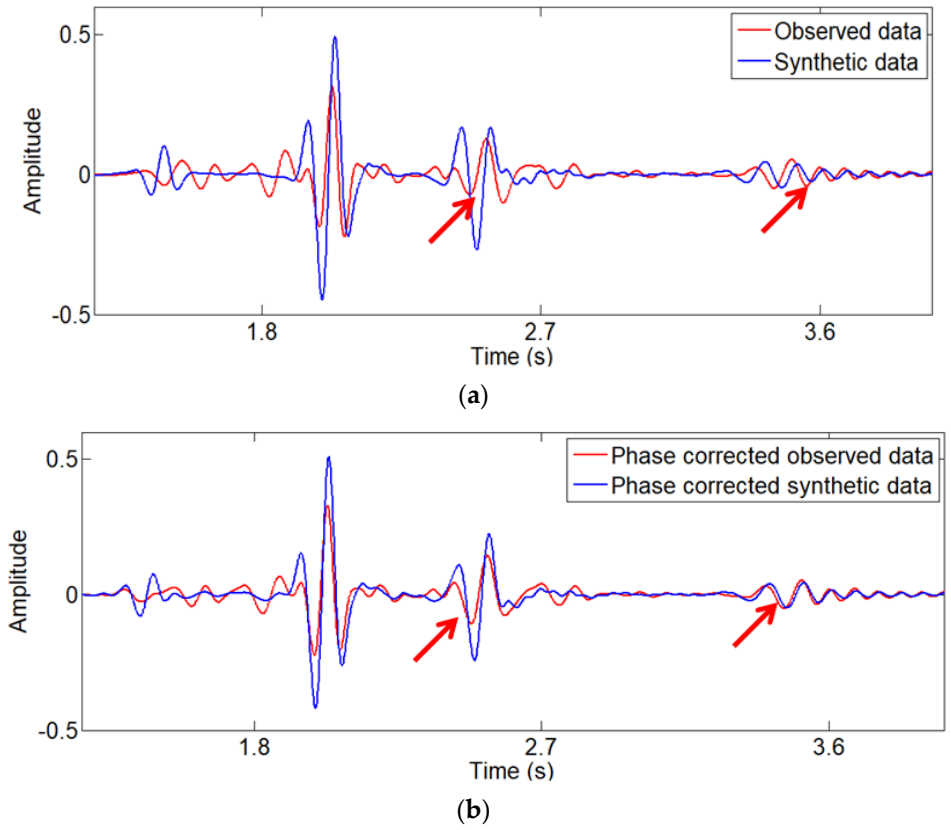

Figure 3. Seismic waveforms. (**a**) Measured and synthetic data; (**b**) phase-corrected measured and synthetic data.

3. Review of Elastic Full Waveform Inversion

The elastic wave equation is the basis of EFWI. In isotropic media, the second order partial differential-based 2D elastic wave equations can be written as,

$$\begin{cases} \rho \frac{\partial^2 \mathbf{u}_x}{\partial t^2} = \frac{\partial \boldsymbol{\sigma}_{xx}}{\partial x} + \frac{\partial \boldsymbol{\sigma}_{xz}}{\partial z} \\ \rho \frac{\partial^2 \mathbf{u}_z}{\partial t^2} = \frac{\partial \boldsymbol{\sigma}_{xz}}{\partial x} + \frac{\partial \boldsymbol{\sigma}_{zz}}{\partial z} \\ \boldsymbol{\sigma}_{xx} = (\boldsymbol{\lambda} + 2\boldsymbol{\mu}) \frac{\partial \mathbf{u}_x}{\partial x} + \boldsymbol{\lambda} \frac{\partial \mathbf{u}_z}{\partial z} \\ \boldsymbol{\sigma}_{zz} = (\boldsymbol{\lambda} + 2\boldsymbol{\mu}) \frac{\partial \mathbf{u}_z}{\partial z} + \boldsymbol{\lambda} \frac{\partial \mathbf{u}_x}{\partial x} \\ \boldsymbol{\sigma}_{xz} = \boldsymbol{\mu} \left(\frac{\partial \mathbf{u}_x}{\partial z} + \frac{\partial \mathbf{u}_z}{\partial x} \right) \end{cases} \tag{5}$$

where $\boldsymbol{\lambda}$ and $\boldsymbol{\mu}$ are Lamé coefficients; ρ is density, which is taken as a constant value ($\rho = 2$ g/cm^3) in the tests of EFWI. In Equation (5), the $\mathbf{u} = [\mathbf{u}_x, \mathbf{u}_z]$ and $\boldsymbol{\sigma} = [\boldsymbol{\sigma}_{xx}, \boldsymbol{\sigma}_{zz}, \boldsymbol{\sigma}_{xz}]$ are displacement components and stress components, respectively.

The misfit of EFWI is to measure the elastic seismic data residuals between the measured and synthetic data as follows [8,11]:

$$J(\mathbf{m}) = \frac{1}{2} \sum_{ns} \sum_{nr} \int \|\mathbf{u} - \mathbf{d}\|_2^2 dt, \tag{6}$$

where ns, nr indicate the number of shots and receivers, respectively; $\mathbf{u}, \mathbf{d}$ are the time-domain measured and synthetic elastic seismic data, which contain horizontal and vertical components $\mathbf{u} = [\mathbf{u}_x, \mathbf{u}_z], \mathbf{d} = [\mathbf{d}_x, \mathbf{d}_z]$. The EFWI misfit can be minimized by updating the elastic parameters with an optimization algorithm. The gradients of the elastic parameters can be expressed as follows,

$$\begin{cases} \frac{\partial J(\mathbf{m})}{\partial \boldsymbol{\lambda}} = -\sum_{ns} \int \left(\frac{\partial \overrightarrow{\mathbf{u}}_x}{\partial x} + \frac{\partial \overrightarrow{\mathbf{u}}_z}{\partial z} \right) \left(\frac{\partial \overleftarrow{\mathbf{u}}_x}{\partial x} + \frac{\partial \overleftarrow{\mathbf{u}}_z}{\partial z} \right) dt \\ \frac{\partial J(\mathbf{m})}{\partial \boldsymbol{\mu}} = -\sum_{ns} \int \left(\frac{\partial \overrightarrow{\mathbf{u}}_x}{\partial z} + \frac{\partial \overrightarrow{\mathbf{u}}_z}{\partial x} \right) \left(\frac{\partial \overleftarrow{\mathbf{u}}_x}{\partial z} + \frac{\partial \overleftarrow{\mathbf{u}}_z}{\partial x} \right) + 2 \left(\frac{\partial \overrightarrow{\mathbf{u}}_x}{\partial x} \frac{\partial \overleftarrow{\mathbf{u}}_x}{\partial x} + \frac{\partial \overrightarrow{\mathbf{u}}_z}{\partial z} \frac{\partial \overleftarrow{\mathbf{u}}_z}{\partial z} \right) dt \end{cases}, \tag{7}$$

where $\overrightarrow{\mathbf{u}} = \left[\overrightarrow{\mathbf{u}}_x, \overrightarrow{\mathbf{u}}_z \right]$ and $\overleftarrow{\mathbf{u}} = \left[\overleftarrow{\mathbf{u}}_x, \overleftarrow{\mathbf{u}}_z \right]$ are the displacements of the forward and back propagated stress components, respectively. In addition, Lamé coefficients are related to the P and S velocities (V_p, V_s), which can be denoted as follows,

$$\begin{cases} \mathbf{v}_p = \sqrt{\frac{\boldsymbol{\lambda}+2\boldsymbol{\mu}}{\boldsymbol{\rho}}} \\ \mathbf{v}_s = \sqrt{\frac{\boldsymbol{\mu}}{\boldsymbol{\rho}}} \end{cases}. \tag{8}$$

Therefore, the elastic parameters can be denoted by the P and S velocities $\mathbf{m} = \left[\mathbf{v}_p, \mathbf{v}_s \right]$. The gradient for V_p and V_s can be expressed as follows,

$$\begin{cases} \frac{\partial J(\mathbf{m})}{\partial \mathbf{v}_p} = 2\rho\, \mathbf{v}_p \frac{\partial J(\mathbf{m})}{\partial \boldsymbol{\lambda}} \\ \frac{\partial J(\mathbf{m})}{\partial \mathbf{v}_s} = -4\rho\, \mathbf{v}_s \frac{\partial J(\mathbf{m})}{\partial \boldsymbol{\lambda}} + 2\rho\, \mathbf{v}_s \frac{\partial J(\mathbf{m})}{\partial \boldsymbol{\mu}} \end{cases}. \tag{9}$$

4. Frequency-Wavenumber Domain Phase Correction-Based EFWI

The nonlinearity of the conventional EFWI misfit makes the inverted results easily fall into local minima. Therefore, a frequency-wavenumber domain phase correction-based EFWI (PC-EFWI) is proposed to solve this problem, which helps to reduce the phase differences between measured and synthetic data. The proposed PC-EFWI misfit is as follows,

$$J(\mathbf{m}) = \frac{1}{2} \sum_{ns} \iint_{\tau,h} \iint_{\omega,k_x} \left| \tilde{\mathbf{u}} \left(\tilde{\mathbf{A}}_u \right)^{\varepsilon} - \tilde{\mathbf{d}} \left(\tilde{\mathbf{A}}_d \right)^{\varepsilon} \right|^2 d\omega dk_x d\tau dh, \tag{10}$$

where $\tilde{\mathbf{A}}_u = \tilde{\mathbf{u}}^* \tilde{\mathbf{d}} / \left| \tilde{\mathbf{u}} \right| \left| \tilde{\mathbf{d}} \right|$, $\tilde{\mathbf{A}}_d = \tilde{\mathbf{u}} \tilde{\mathbf{d}}^* / \left| \tilde{\mathbf{u}} \right| \left| \tilde{\mathbf{d}} \right|$. Phase correction factor $\varepsilon \in [0,\ 0.5]$ is used to control the amount of phase correction. In Equation (10), if we set $\varepsilon = 0.5$, the misfit only matches the amplitude information, which becomes envelope inversion in the frequency-wavenumber domain [38]. In this way, we can obtain a better initial model with $\varepsilon = 0.5$ for conventional EFWI. Then, we can gradually reduce the phase correction factor to match the phase and amplitude differences at the same time to obtain detailed structures.

The partial derivative of the PC-EFWI misfit is as follows,

$$\frac{\partial J(\mathbf{m})}{\partial \mathbf{m}} = \sum_{ns} \iint_{\tau,h} \iint_{\omega,k_x} \mathrm{Re} \left\{ \left[\tilde{\mathbf{u}} \left(\tilde{\mathbf{A}}_u \right)^{\varepsilon} - \tilde{\mathbf{d}} \left(\tilde{\mathbf{A}}_d \right)^{\varepsilon} \right] \frac{\partial}{\partial \mathbf{m}} \left[\tilde{\mathbf{u}} \left(\tilde{\mathbf{A}}_u \right)^{\varepsilon} - \tilde{\mathbf{d}} \left(\tilde{\mathbf{A}}_d \right)^{\varepsilon} \right]^* \right\} d\omega dk_x d\tau dh, \tag{11}$$

where * means the complex conjugation. Taking a further derivative, we have

$$\frac{\partial J(\mathbf{m})}{\partial \mathbf{m}} = \sum_{ns} \iint_{\tau,h} \iint_{\omega,k_x} \mathrm{Re} \left\{ \begin{array}{l} (1-\varepsilon) \mathbf{H} \left(\tilde{\mathbf{u}}^* \left| \tilde{\mathbf{d}} \right| \right)^{(-\varepsilon)} \left(\left| \tilde{\mathbf{u}} \right| \tilde{\mathbf{d}}^* \right)^{\varepsilon} \frac{\partial \tilde{\mathbf{u}}^*}{\partial \mathbf{m}} + \\ \varepsilon\, \mathbf{H} \tilde{\mathbf{u}}^{*(1-\varepsilon)} \left| \tilde{\mathbf{u}} \right|^{\varepsilon-1} \left| \tilde{\mathbf{d}} \right|^{(-\varepsilon)} \left(\tilde{\mathbf{d}}^* \right)^{\varepsilon} \mathrm{Re} \left(\frac{\tilde{\mathbf{u}}}{|\tilde{\mathbf{u}}|} \frac{\partial \tilde{\mathbf{u}}^*}{\partial \mathbf{m}} \right) - \\ \varepsilon\, \mathbf{H} \left(\tilde{\mathbf{u}}^* \right)^{(\varepsilon-1)} \tilde{\mathbf{d}}^* \tilde{\mathbf{d}}^{\varepsilon} \left(\left| \tilde{\mathbf{u}} \right| \left| \tilde{\mathbf{d}} \right| \right)^{(-\varepsilon)} \frac{\partial \tilde{\mathbf{u}}^*}{\partial \mathbf{m}} + \\ \varepsilon\, \mathbf{H} \tilde{\mathbf{d}}^* \left(\tilde{\mathbf{u}}^* \tilde{\mathbf{d}} \right)^{\varepsilon} \left| \tilde{\mathbf{u}} \right|^{(-\varepsilon-1)} \left| \tilde{\mathbf{d}} \right|^{(-\varepsilon)} \mathrm{Re} \left(\frac{\tilde{\mathbf{u}}}{|\tilde{\mathbf{u}}|} \frac{\partial \tilde{\mathbf{u}}^*}{\partial \mathbf{m}} \right) \end{array} \right\} d\omega dk_x d\tau dh, \tag{12}$$

where $\mathbf{H} = \tilde{\mathbf{u}}\left(\tilde{\mathbf{A}}_u\right)^{\varepsilon} - \tilde{\mathbf{d}}\left(\tilde{\mathbf{A}}_d\right)^{\varepsilon}$. The gradient of the PC-EFWI misfit is as follows,

$$\frac{\partial J(\mathbf{m})}{\partial \mathbf{m}} = \sum_{ns} \iint_{\tau,h} \iint_{\omega,k_x} \frac{1}{\left|\tilde{\mathbf{u}}\right|^2 \left(\left|\tilde{\mathbf{u}}\right| \left|\tilde{\mathbf{d}}\right|\right)^{\varepsilon}} \mathrm{Re}\left\{ \begin{array}{l} (1-\varepsilon)\,\mathbf{H}\left|\tilde{\mathbf{u}}\right|^2 \left(\tilde{\mathbf{u}}\tilde{\mathbf{d}}^*\right)^{\varepsilon} \frac{\partial \tilde{\mathbf{u}}^*}{\partial \mathbf{m}} + \\ \tilde{\mathbf{u}}\mathrm{Re}\left[\varepsilon\,\mathbf{H}\tilde{\mathbf{u}}^* \left(\tilde{\mathbf{u}}\tilde{\mathbf{d}}^*\right)^{\varepsilon}\right] \frac{\partial \tilde{\mathbf{u}}^*}{\partial \mathbf{m}} - \\ \varepsilon\,\mathbf{H}\tilde{\mathbf{u}}\tilde{\mathbf{d}}^* \left(\tilde{\mathbf{u}}^*\tilde{\mathbf{d}}\right)^{\varepsilon} \frac{\partial \tilde{\mathbf{u}}^*}{\partial \mathbf{m}} + \\ \tilde{\mathbf{u}}\mathrm{Re}\left[\varepsilon\,\mathbf{H}\,\tilde{\mathbf{d}}^* \left(\tilde{\mathbf{u}}^*\tilde{\mathbf{d}}\right)^{\varepsilon}\right] \frac{\partial \tilde{\mathbf{u}}^*}{\partial \mathbf{m}} \end{array} \right\} d\omega dk_x d\tau dh. \tag{13}$$

According to Equation (1), the final gradient of the PC-EFWI misfit is as follows,

$$\frac{\partial J(\mathbf{m})}{\partial \mathbf{m}} = \sum_{ns} \int_t \mathrm{Re}\left\{ F_{2D}^* \left\{ \begin{array}{l} \frac{(1-\varepsilon)\mathbf{H}\left|\tilde{\mathbf{u}}\right|^2 \left(\tilde{\mathbf{u}}\tilde{\mathbf{d}}^*\right)^{\varepsilon}}{\left|\tilde{\mathbf{u}}\right|^2 \left(\left|\tilde{\mathbf{u}}\right| \left|\tilde{\mathbf{d}}\right|\right)^{\varepsilon}} + \frac{\tilde{\mathbf{u}}\mathrm{Re}\left[\varepsilon\,\mathbf{H}\tilde{\mathbf{u}}^* \left(\tilde{\mathbf{u}}\tilde{\mathbf{d}}^*\right)^{\varepsilon}\right]}{\left|\tilde{\mathbf{u}}\right|^2 \left(\left|\tilde{\mathbf{u}}\right| \left|\tilde{\mathbf{d}}\right|\right)^{\varepsilon}} - \\ \frac{\varepsilon\,\mathbf{H}\tilde{\mathbf{u}}\tilde{\mathbf{d}}^* \left(\tilde{\mathbf{u}}^*\tilde{\mathbf{d}}\right)^{\varepsilon}}{\left|\tilde{\mathbf{u}}\right|^2 \left(\left|\tilde{\mathbf{u}}\right| \left|\tilde{\mathbf{d}}\right|\right)^{\varepsilon}} + \frac{\tilde{\mathbf{u}}\mathrm{Re}\left[\varepsilon\,\mathbf{H}\,\tilde{\mathbf{d}}^* \left(\tilde{\mathbf{u}}^*\tilde{\mathbf{d}}\right)^{\varepsilon}\right]}{\left|\tilde{\mathbf{u}}\right|^2 \left(\left|\tilde{\mathbf{u}}\right| \left|\tilde{\mathbf{d}}\right|\right)^{\varepsilon}} \end{array} \right\} \frac{\partial \mathbf{u}}{\partial \mathbf{m}}\, dt. \right. \tag{14}$$

Additionally, the adjoint source is as follows,

$$f_s = F_{2D}^* \left\{ \frac{(1-\varepsilon)\mathbf{H}\left|\tilde{\mathbf{u}}\right|^2 \left(\tilde{\mathbf{u}}\tilde{\mathbf{d}}^*\right)^{\varepsilon} + \tilde{\mathbf{u}}\mathrm{Re}\left[\varepsilon\,\mathbf{H}\tilde{\mathbf{u}}^* \left(\tilde{\mathbf{u}}\tilde{\mathbf{d}}^*\right)^{\varepsilon}\right] - \varepsilon\,\mathbf{H}\tilde{\mathbf{u}}\tilde{\mathbf{d}}^* \left(\left(\tilde{\mathbf{u}}^*\right)^{\varepsilon}\tilde{\mathbf{d}}^{\varepsilon}\right) + \tilde{\mathbf{u}}\mathrm{Re}\left[\varepsilon\,\mathbf{H}\,\tilde{\mathbf{d}}^* \left(\tilde{\mathbf{u}}^*\tilde{\mathbf{d}}\right)^{\varepsilon}\right]}{\beta + \left|\tilde{\mathbf{u}}\right|^2 \left(\left|\tilde{\mathbf{u}}\right| \left|\tilde{\mathbf{d}}\right|\right)^{\varepsilon}} \right\} \tag{15}$$

where β is a small positive number to avoid dividing over zero. Therefore, the PC-EFWI gradients can be obtained by correlating forward and backward wave-fields.

5. Numerical Test

In this section, we apply complex modified Marmousi models to test the frequency-wavenumber domain phase correction-based elastic full waveform inversion (PC-EFWI). The Marmousi model consists of various complex geological structures, such as anticlines, faults, angular unconformities, and oil reservoirs. Figure 4 shows that the oil reservoir is deep in the Marmousi model and overlaid by complex geological structures. However, the conventional EFWI is challenging to invert the deep oil reservoir, especially when seismic data lack low-frequency components. In this case, the Marmousi velocity models are 1.2 km × 3.6 km, and their initial models are shown in Figure 5. The acquisition system consists of 40 seismic sources and 240 receivers on the top of the velocity model. This article uses a low−cut 5 Hz Ricker wavelet with a peak frequency of 12 Hz to test the low-frequency dependence of the PC-EFWI method. In addition, we first use low−frequency data (5–10 Hz) to recover macro structures. Then, we use it as the initial model for high−frequency data (5–15 Hz) conventional EFWI.

The conventional EFWI results are shown in Figure 6. Compared to the accurate Marmousi models, the conventional EFWI results produce a cluster of anomaly values and artifacts on the left side of the Marmousi velocity models. This is mainly because the conventional EFWI suffers from severe cycle skipping. Then, we use high-frequency seismic data to invert the detailed geological structures with Figure 6 as the initial model. According to Figures 6 and 7, if the low-frequency EFWI produces cycle skipping, the high-frequency data-based EFWI will also produce errors. Therefore, it is essential to use new methods to recover the low-wavenumber components of the velocity models.

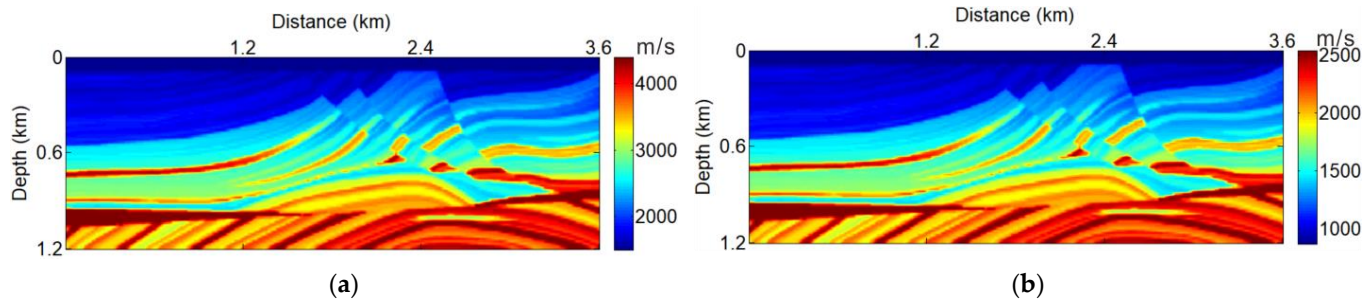

Figure 4. True velocity models; (**a**) V_p; (**b**) V_s.

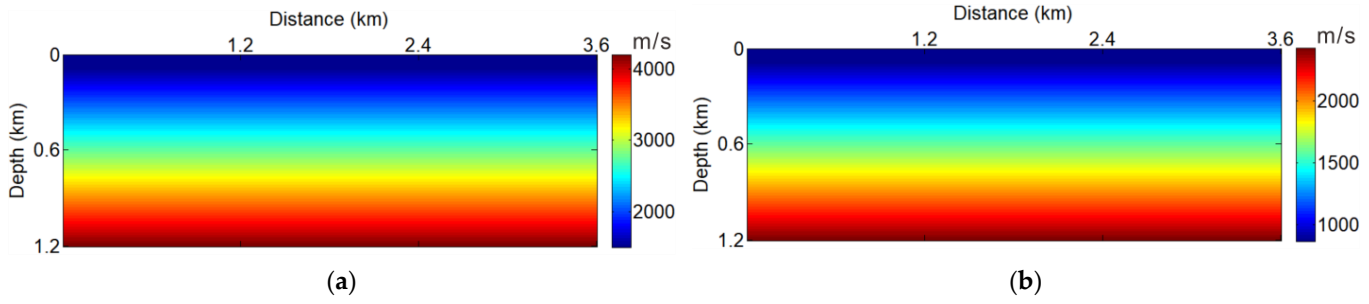

Figure 5. Initial velocity models; (**a**) V_p; (**b**) V_s.

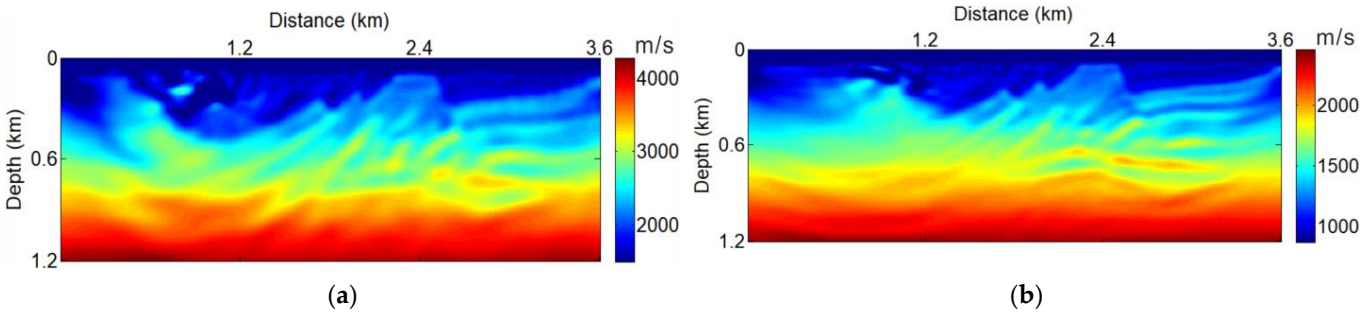

Figure 6. Conventional EFWI results with low-frequency data (5–10 Hz); (**a**) V_p; (**b**) V_s.

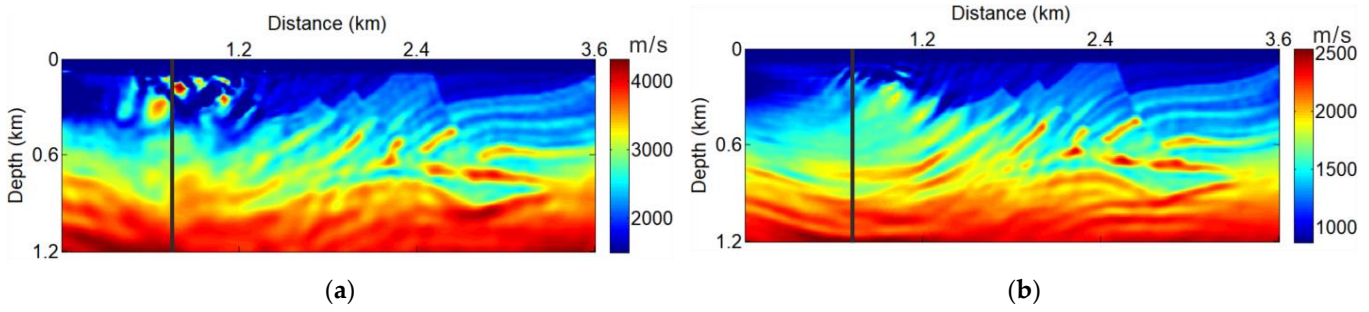

Figure 7. Conventional EFWI results with high-frequency data (5–15 Hz) using Figure 6 as the initial model; (**a**) V_p; (**b**) V_s.

Now, the low-frequency seismic data-based PC-EFWI results with phase correction factor $\varepsilon = 0.5$ are shown in Figure 8. Compared to Figure 6, the geological macro structures of the Marmousi model inverted by PC-EFWI (Figure 8) seem better than the conventional EFWI result, because when the phase correction factor $\varepsilon = 0.5$, the PC-EFWI misfit becomes a pure amplitude misfit, similar to the envelope misfit with a solid ability to recover macro structures. In addition, we can gradually reduce the phase correction factor to match the phase differences between the measured and synthetic data. For example, we then set $\varepsilon = 0.3$ and use Figure 8 as the initial velocity model to obtain detailed geological

structures, shown in Figure 9. After that, we can use the inverted background Marmousi model (Figure 9) as the initial model for the conventional EFWI to invert detailed geological structures (Figures 10 and 11). A comparison of Figures 7 and 11 shows that the PC-EFWI can better recover the oil reservoir, and the deep geological structures can be seen clearly.

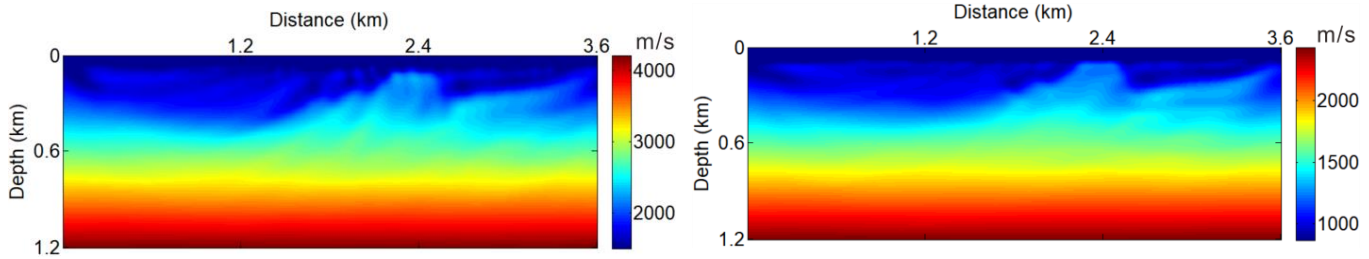

(**a**) (**b**)

Figure 8. Low-frequency data (5–10 Hz) based PC-EFWI results with phase correction factor $\varepsilon = 0.5$; (**a**) V_p; (**b**) V_s.

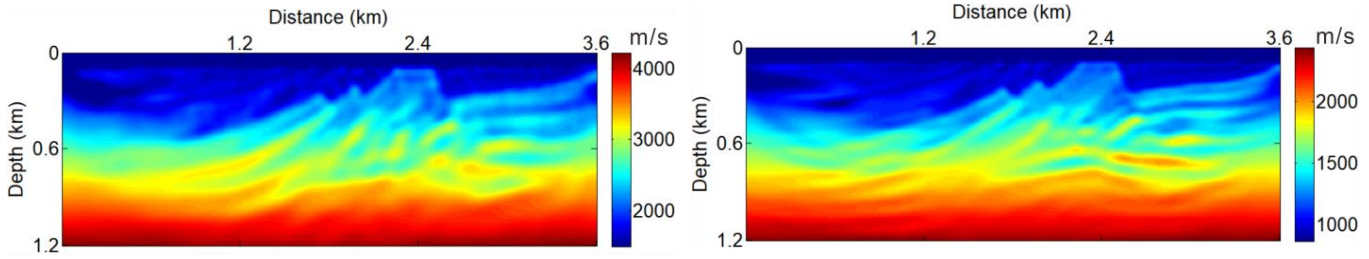

(**a**) (**b**)

Figure 9. Low-frequency data (5–10 Hz) based PC-EFWI results with phase correction factor $\varepsilon = 0.3$ using Figure 8 for initial velocity models; (**a**) V_p; (**b**) V_s.

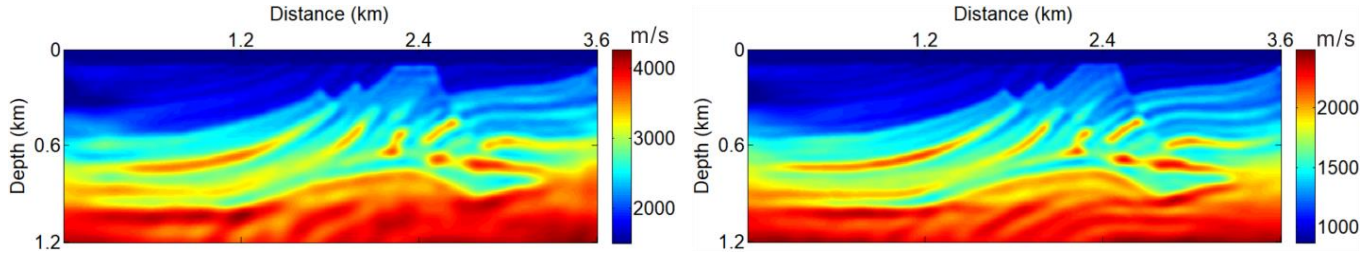

(**a**) (**b**)

Figure 10. Low-frequency data (5–10 Hz) based conventional EFWI results using Figure 9 for the initial velocity models. (**a**) V_p; (**b**) V_s.

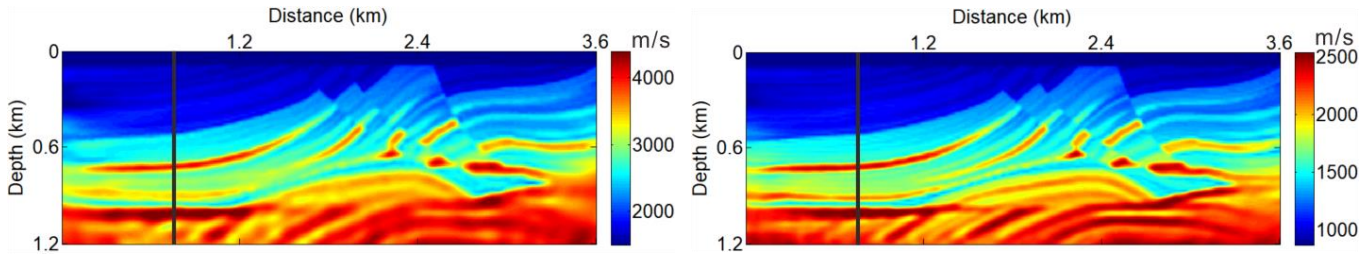

(**a**) (**b**)

Figure 11. High-frequency data (5–10 Hz) based EFWI results using Figure 10 as the initial velocity model; (**a**) V_p; (**b**) V_s.

The inverted velocity profiles with conventional EFWI and PC-EFWI are shown in Figure 12. Figure 12a,b show that the conventional EFWI has severe cycle skipping, and the final inverted models are deplorable. The comparison results in Figure 12a–d show that the V_p and V_s of PC-EFWI + EFWI results are more similar to the accurate elastic velocity of V_p and V_s. The velocity comparison in Figure 12 shows that the frequency-wavenumber domain PC-EFWI misfit can successfully build better initial models for EFWI and mitigate the cycle skipping.

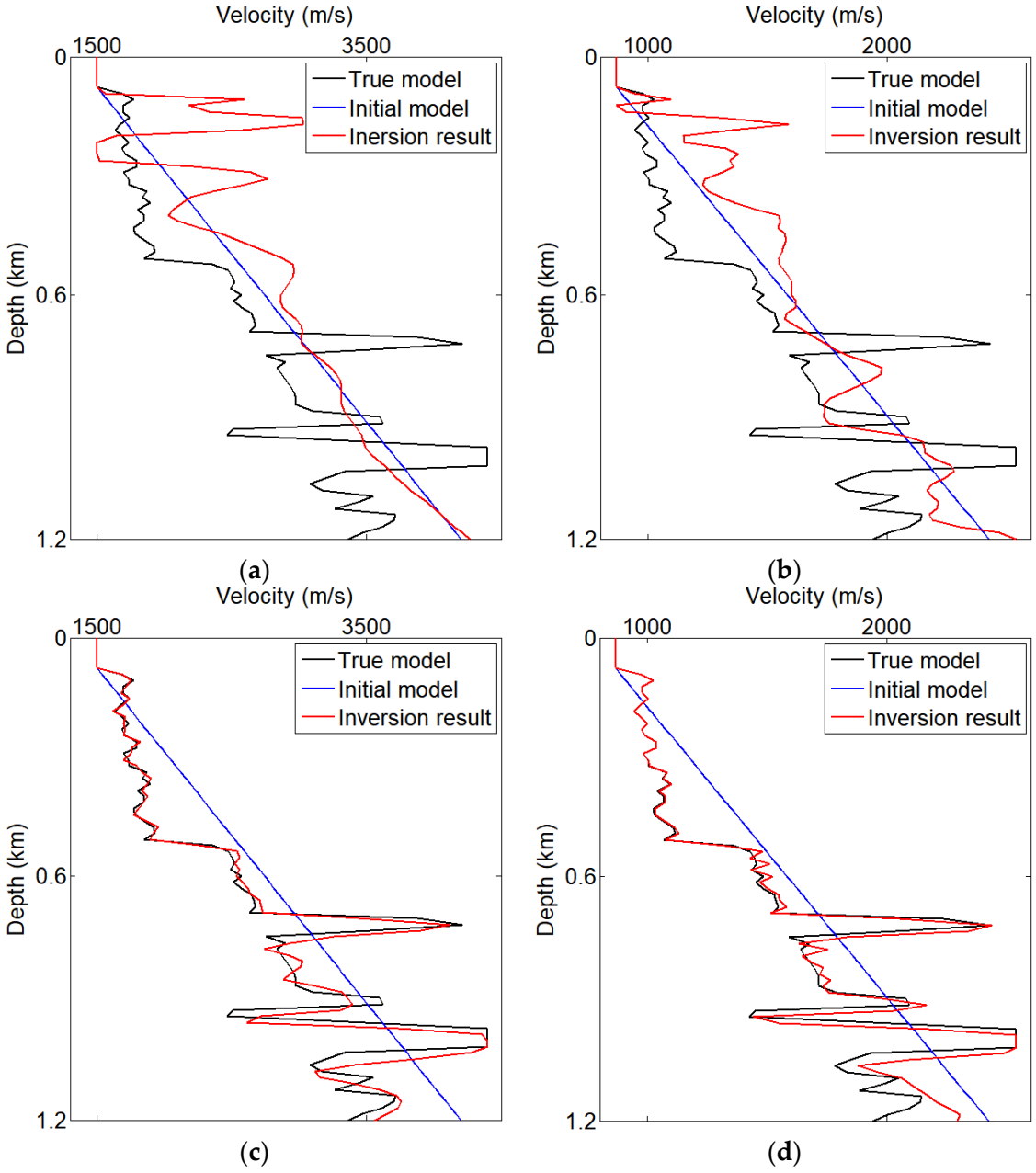

Figure 12. The elastic velocity profiles (at 0.75 km in the inverted Marmousi models in Figures 7 and 11, respectively); (**a**,**b**) are the conventional EFWI results of V_p and V_s; (**c**,**d**) are the PC-EFWI + EFWI results of the V_p and V_s.

6. Discussion

In this article, the 2-D window size for PC-EFWI is an important parameter, which is similar to the window size for Short-time Fourier transform (STFT). In STFT, the time and frequency resolution is a trade-off problem. Although a narrow-width window results

in a better resolution in the time domain, it generates a poor resolution in the frequency domain, and vice versa. Similarly, although a narrow-width 2-D window results in a better exhibition of local-scale characteristics in the time-space domain, it can not encompass a complete waveform of seismic events, and vice versa. Therefore, the choice of 2-D window size involves a certain amount of experience. In this article, the window length in the time direction is 0.36 s, and the window length in the distance direction is 0.6 km (Figure 2). In addition, the PC-EFWI misfit needs to calculate the forward and inverse window based 2-D Fourier transform both of synthetic and measured data, which requires a substantial amount of computing resources. Fortunately, a large sliding step length can greatly improve calculation efficiency. Additionally, the sliding step length of the 2D window is 1/10 of the window length in the time and distance directions. In this way, an appropriate sliding step length can not only ensure the accuracy of the window based 2-D Fourier transform, but also improve the calculation efficiency.

7. Conclusions

We proposed a frequency-wavenumber domain PC-EFWI to invert for the low-wavenumber components of subsurface structures. With a phase correction factor adopted in the PC-EFWI misfit, we can flexibly adjust the phase differences between the measured and synthetic data to reduce the nonlinearity of the EFWI misfit, which mitigates the cycle skipping problem to a large extent. For the multistage strategy, we first use a large phase correction factor to eliminate phase differences in the PC-EFWI misfit, which is suitable to invert the macro structures of the complex Marmousi models. Then, we can gradually reduce the phase correction factor to form a more robust multistage inversion strategy to obtain detailed geological structures. Numerical tests show that the frequency-wavenumber domain PC-EFWI method can successfully build accurate background velocity models and mitigate cycle skipping of the EFWI.

Author Contributions: Conceptualization, Y.H.; methodology, Y.H.; software, Y.H.; validation, Y.H., L.-Y.F., Q.L., W.D. and L.H.; formal analysis, Y.H. and L.-Y.F.; resources, Y.H.; data curation, Y.H. and L.-Y.F.; writing-original draft preparation, Y.H. and L.-Y.F.; writing-review and editing, Y.H., L.-Y.F., Q.L., W.D. and L.H.; visualization, Y.H.; supervision, L.-Y.F.; project administration, Y.H., L.-Y.F., Q.L., W.D. and L.H.; funding acquisition, Y.H., L.-Y.F., Q.L. and L.H. All authors have read and agreed to the published version of the manuscript.

Funding: This work is supported by the National Natural Science Foundation of China (Grant No. 42130805, 42104116, 41821002, 42074132), Jiangsu Key R&D Plan (Grant No. BE2020644), the Natural Science Foundation of Jiangsu Province (Grant No. BK20200644), and the China Postdoctoral Science Foundation (Grant No. 2021M703580).

Data Availability Statement: The data associated with this paper are available by contacting the corresponding author.

Acknowledgments: This work is also supported by the Priority Academic Program Development of Jiangsu Higher Education Institutions.

Conflicts of Interest: The authors declare no conflict of interest.

References

1. Baysal, E.; Kosloff, D.D.; Sherwood, J.W.C. Reverse-Time Migration. *Geophysics* **1983**, *48*, 1514–1524. [CrossRef]
2. Yao, D.; Zhou, X. One-Way Elastic Wave Reverse-Time Migration. *Geophys. J. Int.* **1993**, *112*, 381–384. [CrossRef]
3. Gu, Z.; Wu, R.-S. Internal Multiple Removal and Illumination Correction for Seismic Imaging. *IEEE Trans. Geosci. Remote Sens.* **2021**, 1–11. [CrossRef]
4. Fang, J.; Shi, Y.; Zhou, H.; Chen, H.; Zhang, Q.; Wang, N. A High-Precision Elastic Reverse-Time Migration for Complex Geologic Structure Imaging in Applied Geophysics. *Remote Sens.* **2022**, *14*, 3542. [CrossRef]
5. Hu, Y.; Chen, T.; Fu, L.-Y.; Wu, R.-S.; Xu, Y.; Han, L.; Huang, X. A 2-D Local Correlative Misfit for Least-Squares Reverse Time Migration with Sparsity Promotion. *IEEE Trans. Geosci. Rem. Sens.* **2022**, *60*, 1–13. [CrossRef]
6. Lailly, P.; Bednar, J. The seismic inverse problems as a sequence of before stack migration. In *Conference on Inverse Scattering Theory and Application, Society of Industrial and Applied Mathematics*; SIAM: Philadelphia, PA, USA, 1983; pp. 206–220.

7. Tarantola, A. Inversion of seismic reflection data in the acoustic approximation. *Geophysics* **1984**, *49*, 1259–1266. [CrossRef]
8. Pratt, R.G.; Shin, C.; Hicks, G.J. Gauss-Newton and full Newton methods in frequency-space seismic waveform inversion. *Geophys. J. Int.* **1998**, *133*, 341–362. [CrossRef]
9. Plessix, R.E. A review of the adjoint-state method for computing the gradient of a functional with geophysical applications. *Geophys. J. Int.* **2006**, *167*, 495–503. [CrossRef]
10. Fichtner, A.; Trampert, J. Resolution analysis in full waveform inversion. *Geophys. J. Int.* **2011**, *187*, 1604–1624. [CrossRef]
11. Mora, P. Nonlinear two-dimensional elastic inversion of multioffset seismic data. *Geophysics* **1987**, *52*, 1211–1228. [CrossRef]
12. Shin, C.; Cha, Y.H. Waveform inversion in the Laplace domain. *Geophys. J. Int.* **2008**, *173*, 922–931. [CrossRef]
13. Virieux, J.; Operto, S. An overview of full-waveform inversion in exploration geophysics. *Geophysics* **2009**, *74*, WCC127–WCC152. [CrossRef]
14. Van Leeuwen, T.; Mulder, W.A. A correlation-based misfit criterion for wave-equation traveltime tomography. *Geophys. J. Int.* **2010**, *182*, 1383–1394. [CrossRef]
15. Liu, Y.; Teng, J.; Xu, T.; Wang, Y.; Liu, Q.; Badal, J. Robust time-domain full waveform inversion with normalized zero-lag cross-correlation objective function. *Geophys. J. Int.* **2016**, *209*, 106–122. [CrossRef]
16. Métivier, L.; Brossier, R.; Mérigot, Q.; Oudet, E.; Virieux, J. Measuring the misfit between seismograms using an optimal transport distance: Application to full waveform inversion. *Geophys. J. Int.* **2017**, *205*, 332–364. [CrossRef]
17. Geng, Y.; Pan, W.; Innanen, K.A. Frequency-domain full-waveform inversion with non-linear descent directions. *Geophys. J. Int.* **2018**, *213*, 739–756. [CrossRef]
18. Chi, B.X.; Dong, L.G.; Liu, Y.Z. Full waveform inversion method using envelope objective function without low frequency data. *J. App. Geophy.* **2014**, *109*, 36–46. [CrossRef]
19. Wu, R.S.; Luo, J.R.; Wu, B.Y. Seismic envelope inversion and modulation signal model. *Geophysics* **2014**, *79*, WA13–WA24. [CrossRef]
20. Bharadwaj, P.; Mulder, W.; Drijkoningen, G. Full waveform inversion with an auxiliary bump functional. *Geophys. J. Int.* **2016**, *206*, 1076–1092. [CrossRef]
21. Wu, R.; Chen, G. New Fréchet derivative for envelope data and multi-scale envelope inversion. In Proceedings of the 79th EAGE Conference and Exhibition, Paris, France, 12–15 June 2017.
22. Hu, Y.; Han, L.; Xu, Z.; Zhang, F.; Zeng, J. Adaptive multi-step full waveform inversion based on waveform mode decomposition. *J. App. Geophys.* **2017**, *139*, 195–210. [CrossRef]
23. Hu, Y.; Wu, R.S.; Huang, X.; Long, Y.; Xu, Y.; Han, L.G. Phase-amplitude-based polarized direct envelope inversion in the time-frequency domain. *Geophysics* **2022**, *87*, R245–R260. [CrossRef]
24. Huang, X.; Eikrem, K.S.; Jakobsen, M.; Nævdal, G. Bayesian full-waveform inversion in anisotropic elastic media using the iterated extended Kalman filter. *Geophysics* **2020**, *85*, C125–C139. [CrossRef]
25. Fang, J.; Zhou, H.; Zhang, Q.; Chen, H.; Sun, P.; Zhang, J.; Zhang, L. The effects of elastic data on acoustic and elastic full waveform inversion. *J. Appl. Geophys.* **2020**, *172*, 103876. [CrossRef]
26. Huang, X.; Greenhalgh, S.; Han, L.; Liu, X. Generalized Effective Biot Theory and Seismic Wave Propagation in Anisotropic, Poroviscoelastic Media. *J. Geophys. Res. Solid Earth* **2022**, *127*, e2021JB023590. [CrossRef]
27. Pan, W.; Ma, N.; Wang, Y. An Envelope Travel-Time Objective Function for Reducing Source–Velocity Trade-Offs in Wave-Equation Tomography. *Remote Sens.* **2022**, *14*, 5223. [CrossRef]
28. Wang, N.; Shi, Y.; Zhou, H. Accurately Stable Q-Compensated Reverse-Time Migration Scheme for Heterogeneous Viscoelastic Media. *Remote Sens.* **2022**, *14*, 4782. [CrossRef]
29. Wenyi, H. FWI without low frequency data-beat tone inversion. In *SEG Technical Program Expanded Abstracts 2014*; Society of Exploration Geophysicists: Houston, TX, USA, 2014; pp. 1116–1120.
30. Shin, C.; Ha, W. A comparison between the behavior of objective functions for waveform inversion in the frequency and Laplace domains. *Geophysics* **2008**, *73*, 119–133. [CrossRef]
31. Chung, W.; Shin, C.; Pyun, S. 2D Elastic Waveform Inversion in the Laplace Domain. *Bull. Seismol. Soc. Am.* **2010**, *100*, 3239–3249. [CrossRef]
32. Alkhalifah, T.; Choi, Y. Taming waveform inversion nonlinearity through phase unwrapping of the model and objective functions. *Geophys. J. Int.* **2012**, *191*, 1171–1178.
33. Jimenez Tejero, C.E.; Sallares, V.; Ranero, C.R. Appraisal of Instantaneous Phase-Based Functions in Adjoint Waveform Inversion. *IEEE Trans. Geosci. Remote Sens.* **2018**, *56*, 5185–5197. [CrossRef]
34. Bunks, C.; Saleck, F.M.; Zaleski, S.; Chavent, G. Multiscale seismic waveform inversion. *Geophysics* **1995**, *60*, 1457–1473. [CrossRef]
35. Sirgue, L.; Pratt, R.G. Efficient waveform inversion and imaging: A strategy for selecting temporal frequencies. *Geophysics* **2004**, *69*, 231–248. [CrossRef]
36. Fichtner, A.; Trampert, J.; Cupillard, P.; Saygin, E.; Taymaz, T.; Capdeville, Y.; Villaseñor, A. Multiscale full waveform inversion. *Geophys. J. Int.* **2013**, *194*, 534–556. [CrossRef]
37. Ying, H.; Zhang, D.; Jianzheng, Y.; Huang, S.; Di, Y.; Ling, X.; Zhang, C.; Qianqing, Q. An efficient multi-scale waveform inversion method in Laplace-Fourier domain. *Pet. Explor. Dev.* **2015**, *42*, 369–378.
38. Fichtner, A.B.; Kennett, L.N.; Igel, H.; Bunge, H. Theoretical background for continental- and global-scale full-waveform inversion in the time-frequency domain. *Geophys. J. Int.* **2008**, *175*, 665–685. [CrossRef]

39. Bozdağ, E.J.; Trampert, T.J. Misfit functions for full waveform inversion based on instantaneous phase and envelope measurements. *Geophys. J. Int.* **2011**, *185*, 845–870. [CrossRef]
40. Chen, G.; Yang, W.; Liu, Y.; Wang, H.; Huang, X. Salt Structure Elastic Full Waveform Inversion Based on the Multiscale Signed Envelope. *IEEE Trans. Geosci. Remote Sens.* **2022**, *60*, 4508912. [CrossRef]
41. Gao, Z.Q.; Pan, Z.B.; Gao, J.H.; Wu, R.S. Frequency Controllable Envelope Operator and Its Application in Multiscale Full-Waveform Inversion. *IEEE Trans. Geosci. Remote Sens.* **2019**, *57*, 683–699. [CrossRef]
42. Chen, G.; Yang, W.; Liu, Y.; Luo, J.; Jing, H. Envelope-Based Sparse-Constrained Deconvolution for Velocity Model Building. *IEEE Trans. Geosci. Remote Sens.* **2022**, *60*, 4501413. [CrossRef]
43. Zhang, P.; Wu, R.-S.; Han, L.-G.; Hu, Y. Elastic direct envelope inversion based on wave mode decomposition for multi-parameter reconstruction of strong-scattering media. *Pet. Sci.* **2022**, *19*, 2046–2063. [CrossRef]
44. Hu, Y.; Fu, L.-Y.; Deng, W.; Li, Q.; Huang, X. Joint Traditional and Reflection Envelope Inversion. *IEEE Geosci. Remote Sens. Lett.* **2022**, *19*, 8025505. [CrossRef]
45. Li, Y.E.; Demanet, L. Full waveform inversion with extrapolated low frequency data. *Geophysics* **2016**, *81*, R339–R348. [CrossRef]
46. Luo, S.; Sava, P. A deconvolution-based objective function for wave-equation inversion. In *SEG Technical Program Expanded Abstracts 2011*; Society of Exploration Geophysicists: Houston, TX, USA, 2011.
47. Zhang, P.; Han, L.; Xu, Z.; Zhang, F.; Wei, Y. Sparse blind deconvolution based low-frequency seismic data reconstruction for multiscale full waveform inversion. *J. Appl. Geophys.* **2017**, *139*, 91–108. [CrossRef]
48. Choi, Y.; Alkhalifah, T. Time-domain full-waveform inversion of exponentially damped wavefield using the deconvolution-based objective function. *Geophysics* **2018**, *83*, R77–R88. [CrossRef]
49. Chen, G.; Yang, W.; Wang, H.; Zhou, H.; Huang, X. Elastic Full Waveform Inversion based on Full-Band Seismic Data Reconstructed by Dual Deconvolution. *IEEE Geosci. Remote Sens. Lett.* **2022**, *19*, 8028205. [CrossRef]
50. Sun, H.; Demanet, L. Low-frequency extrapolation with deep learning. In *SEG Technical Program Expanded Abstracts 2018*; Society of Exploration Geophysicists: Houston, TX, USA, 2018.
51. Sun, H.; Demanet, L. Extrapolated full-waveform inversion with deep learning. *Geophysics* **2020**, *85*, R275–R288. [CrossRef]
52. Fang, J.; Zhou, H.; Li, Y.E.; Zhang, Q.; Zhang, J. Data-driven low-frequency signal recovery using deep learning predictions in full-waveform inversion. *Geophysics* **2020**, *85*, A37–A43. [CrossRef]
53. Zhang, Z.; Alkhalifah, T. Regularized elastic full-waveform inversion using deep learning. In *Advances in Subsurface Data Analytics*; Elsevier: Amsterdam, The Netherlands, 2022; pp. 219–250.
54. Warner, M.; Guasch, L. Adaptive waveform inversion: Theory. *Geophysics* **2016**, *81*, R429–R445. [CrossRef]
55. Zhu, H.; Fomel, S. Building good starting models for full-waveform inversion using adaptive matching filtering misfit. *Geophysics* **2016**, *81*, U61–U72. [CrossRef]
56. Sun, B.; Alkhalifah, T. Adaptive Traveltime Inversion. *Geophysics* **2019**, *84*, U13–U29. [CrossRef]
57. Sun, B.; Alkhalifah, T.A. Joint Minimization of the Mean and Information Entropy of the Matching Filter Distribution for a Robust Misfit Function in Full-Waveform Inversion. *IEEE Trans. Geosci. Remote Sens.* **2020**, *58*, 4704–4720. [CrossRef]
58. Wang, J.; Yang, D.; Jing, H.; Wu, H. Full waveform inversion based on the ensemble Kalman filter method using uniform sampling without replacement. *Sci. Bull.* **2019**, *64*, 321–330. [CrossRef]
59. Solano, C.A.P.; Donno, D.; Chauris, H. Alternative waveform inversion for surface wave analysis in 2-D media. *Geophys. J. Int.* **2014**, *198*, 1359–1372. [CrossRef]
60. Fu, L.; Guo, B.; Schuster, G.T. Multiscale phase inversion of seismic data. *Geophysics* **2017**, *83*, R159–R171. [CrossRef]
61. Hu, Y.; Han, L.G.; Yu, J.L.; Chen, R.D. Time-frequency domain multi-scale full waveform inversion based on adaptive non-stationary phase correction. *Chin. J. Geophys.* **2018**, *61*, 2969–2988. [CrossRef]
62. Chen, Y.; Feng, Z.; Fu, L.; AlTheyab, A.; Feng, S.; Schuster, G. Multiscale reflection phase inversion with migration deconvolution. *Geophysics* **2019**, *85*, R55–R73. [CrossRef]